SCIENTIFIC REPORTS

OPEN

Received: 22 April 2015
Accepted: 24 June 2015
Published: 28 August 2015

Peculiarity of Two Thermodynamically-Stable Morphologies and Their Impact on the Efficiency of Small Molecule Bulk Heterojunction Solar Cells

Nuradhika Herath[1], Sanjib Das[2], Jong K. Keum[3], Jiahua Zhu[3], Rajeev Kumar[3,5], Ilia N. Ivanov[3], Bobby G. Sumpter[3,5], James F. Browning[4], Kai Xiao[3], Gong Gu[2], Pooran Joshi[6], Sean Smith[7] & Valeria Lauter[1]

Structural characteristics of the active layers in organic photovoltaic (OPV) devices play a critical role in charge generation, separation and transport. Here we report on morphology and structural control of *p*-DTS(FBTTh$_2$)$_2$:PC$_{71}$BM films by means of thermal annealing and 1,8-diiodooctane (DIO) solvent additive processing, and correlate it to the device performance. By combining surface imaging with nanoscale *depth-sensitive* neutron reflectometry (NR) and X-ray diffraction, three-dimensional morphologies of the films are reconstituted with information extending length scales from nanometers to microns. DIO promotes the formation of a well-mixed donor-acceptor vertical phase morphology with a large population of *small p*-DTS(FBTTh$_2$)$_2$ nanocrystals arranged in an elongated domain network of the film, thereby enhancing the device performance. In contrast, films without DIO exhibit three-sublayer vertical phase morphology with phase separation in agglomerated domains. Our findings are supported by thermodynamic description based on the Flory-Huggins theory with quantitative evaluation of pairwise interaction parameters that explain the morphological changes resulting from thermal and solvent treatments. Our study reveals that vertical phase morphology of small-molecule based OPVs is significantly different from polymer-based systems. The significant enhancement of morphology and information obtained from theoretical modeling may aid in developing an optimized morphology to enhance device performance for OPVs.

Organic photovoltaics (OPVs) are promising light conversion technologies expecting to meet the demands of low manufacturing costs, green technology, and efficient operation under low-light conditions[1,2]. Major breakthroughs in OPV performance have been achieved by incorporating new conjugated polymers or small molecules into bulk heterojunction (BHJ) devices enabling further optimization of active layer morphology[3–7]. During solution casting of the OPV layer, electron donor (ED) and acceptor (EA) molecules

[1]Quantum Condensed Matter Division, Oak Ridge National Laboratory, Oak Ridge, TN 37831, USA. [2]Department of Electrical Engineering and Computer Science, University of Tennessee, Knoxville, TN 37996, USA. [3]Center for Nanophase Materials Sciences, Oak Ridge National Laboratory, Oak Ridge, TN 37831, USA. [4]Chemical and Engineering Materials Division, Oak Ridge National Laboratory, Oak Ridge, TN 37831, USA. [5]Computer Science and Mathematics Division, Oak Ridge National Laboratory, Oak Ridge, TN, 37831, USA. [6]Materials Science and Technology Division, Oak Ridge National Laboratory, Oak Ridge, TN 37831, USA. [7]School of Chemical Engineering, UNSW Australia, Sydney, NSW 2052, Australia. Correspondence and requests for materials should be addressed to N.H. (email: herathnn@ornl.gov) or V.L. (email: lauterv@ornl.gov)

undergo self-assembly leading to a bicontinuous, interpenetrating network of ED and EA phases, which provide pathways for the transport of electrons and holes. The BHJ ED-EA network with a length scale ranging from nano- to mesoscale is crucial to the power conversion efficiency (PCE) of OPVs[8]. Several successful approaches of optimizing the network morphology include thermal or solvent annealing[9–11], casting from a high boiling point or from a binary solvent, or by introducing processing additives[12–15], all of which improve exciton diffusion-dissociation and charge transport, leading to higher PCE[16–20].

Recently, low band gap conjugated polymer/fullerene[21,22] and small molecule/fullerene[23–31] blends have shown more promising results. The latter system is known to be easier to purify, and the devices show consistently better batch-to-batch reproducibility, higher crystallinity and better performance[28,32,33]. Devices based on the ED:EA system of 7,7′-[4,4-Bis (2-ethylhexyl)-4*H*-silolo[3,2-*b*:4,5-*b*′]dithiophene-2,6-diyl] bis[6-fluoro-4-(5′-hexyl-[2,2′-bithiophen]-5-yl)benzo[*c*][1,2,5]thiadiazole]) (*p*-DTS(FBTTh$_2$)$_2$ and [6,6]-Phenyl C_{72} butyric acid methyl ester ($PC_{71}BM$) have demonstrated PCEs as high as ~9%[25]. Thermal annealing of *p*-DTS(FBTTh$_2$)$_2$:$PC_{71}BM$ further improves the performance through the formation of wire-like 2D crystal domains of *p*-DTS(FBTTh$_2$)$_2$ reaching ~100 nm in length[13]. The results obtained by single crystal x-ray diffraction (SCXRD) and grazing incidence wide angle x-ray scattering (GIWAXS) indicated that *p*-DTS(FBTTh$_2$)$_2$ molecules grew into two-dimensional (2D) columnar arrays with increased π–π overlapping, which leads to improved intermolecular charge transport, and enhanced value of PCE[13]. A processing additive, 1,8-diiodooctane (DIO) enables formation of a well interconnected network of crystalline *p*-DTS(FBTTh$_2$)$_2$ domains with of ~30 nm[14]. It was also shown that the addition of 0.4 vol% of DIO results in different coherent lengths of $PC_{71}BM$ and *p*-DTS(FBTTh$_2$)$_2$ domains[34]. Recent advances in structural study of the polymer/fullerene system have identified the presence of mixed phases containing fullerene molecules dispersed in the donor phase[35,36]. While pure donor and acceptor phases reduce charge recombination by pushing holes away from electrons and, thus, enhancing device performances, the role of a third phase remains unclear[35,36]. Formation of the mixed phases may be expected in SM OPV as well as *p*-DTS(FBTTh$_2$)$_2$ and $PC_{71}BM$ phase-separation during solidification. If one blending component prefers the air/film, bulk or film/substrate interface it may lead to complex vertical phase stratification, including pure or mixed phases with a morphology different from bulk phase of BHJ. Thus, not only the in-plane structure, but also the vertical structure of the SM OPV should be investigated in detail. Highly penetrative and nondestructive neutron reflectometry is an ideal tool for profiling the buried phases and interfacial morphology of *p*-DTS(FBTTh$_2$)$_2$:$PC_{71}BM$ blended films in the direction perpendicular to the film surface down to the substrate. The high contrast in neutron scattering length density (*n*SLD) between *p*-DTS(FBTTh$_2$)$_2$ (1.33×10^{-6} Å^{-2}) (see experimental section) and $PC_{71}BM$ (4.3×10^{-6} Å^{-2})[37] allows clear distinction of the components. While the depth phase morphologies of various conjugated polymer: fullerene derivative OPVs have been successfully described using neutron reflectometry[38–43] or by depth profiling secondary ion mass spectroscopy (DSIMS)[44], investigation of the depth phase morphology of SM OPV has not been reported. Here, we use neutron reflectometry[43] to unfold the depth phase morphology of *p*-DTS(FBTTh$_2$)$_2$ and $PC_{71}BM$ blend and complemented with the use of absorption and photoluminescence spectroscopy, atomic force microscopy (AFM) and X-ray diffraction (XRD) characterizations to correlate the morphology to the OPV device performance after thermal annealing and DIO additive processing. Our results reveal that depth profiles of SM-based systems are different from the polymer-based systems. A thermodynamic description based on Flory-Huggins theory was used to better understand the effect of DIO and thermal annealing on the structure and morphologies of thin active layers, and its relationship with the device performances. Our combined experimental and theoretical approach allows us to demonstrate correlations between the morphology and device performance, as well as to explain origin of different morphologies.

Results and Discussion

Thin films were fabricated by spin casting a solution of *p*-DTS(FBTTh$_2$)$_2$:$PC_{71}BM$ (1.5:1 wt.%)/chlorobenzene onto a sapphire (Al_2O_3) or quartz (SiO_2) substrate. The surface morphologies of *p*-DTS(FBTTh$_2$)$_2$:$PC_{71}BM$ thin films were investigated with AFM in tapping mode. Figure 1 shows AFM images of (a) as-cast, and (c) thermally annealed *p*-DTS(FBTTh$_2$)$_2$:$PC_{71}BM$ films and films with (e) 0.25 vol% DIO and (g) after annealing at 80 °C. The surface of the as-cast sample, as evident from Fig. 1(a), consists of *p*-DTS(FBTTh$_2$)$_2$ and $PC_{71}BM$ molecules in a random arrangement as a uniform mixture. The root mean square roughness (r_{RMS}) of the sample increases from 0.59 nm to 1.75 nm after thermal treatment. The surface of the annealed film consists of domains, which are approximately 500 nm to 1 μm long. The morphology of the surface of the sample with 0.25 vol% DIO (Fig. 1(e)) is drastically different from (a) and (b) without DIO. It is composed of long wire-shape domains extending up to ~200 nm. After the thermal annealing (Fig. 1(g)), the r_{RMS} of the films decreases from ~2.39 nm to ~2.27 nm.

Figure 2 shows the vertical phase morphology of *p*-DTS(FBTTh$_2$)$_2$:$PC_{71}BM$ films, which was investigated using neutron reflectometry. In devices, the active layer is usually spun cast on amorphous PEDOT:PSS layer. However, in previously reported neutron reflectivity experiments, the studies have been performed using BHJ films grown directly on the substrate[38,40,43,45], which have similar surface properties as Al_2O_3 or SiO_2 substrates used in these experiments. Therefore, we primarily compared the neutron reflectometry results from samples directly spin cast on SiO_2 and Al_2O_3 substrates (Fig. S1) and that on PEDOT:PSS layer (Fig. S2). The active layer vertical phase morphologies of the samples are similar indicating that BHJ films fabricated directly on substrates would accurately reflect the vertical

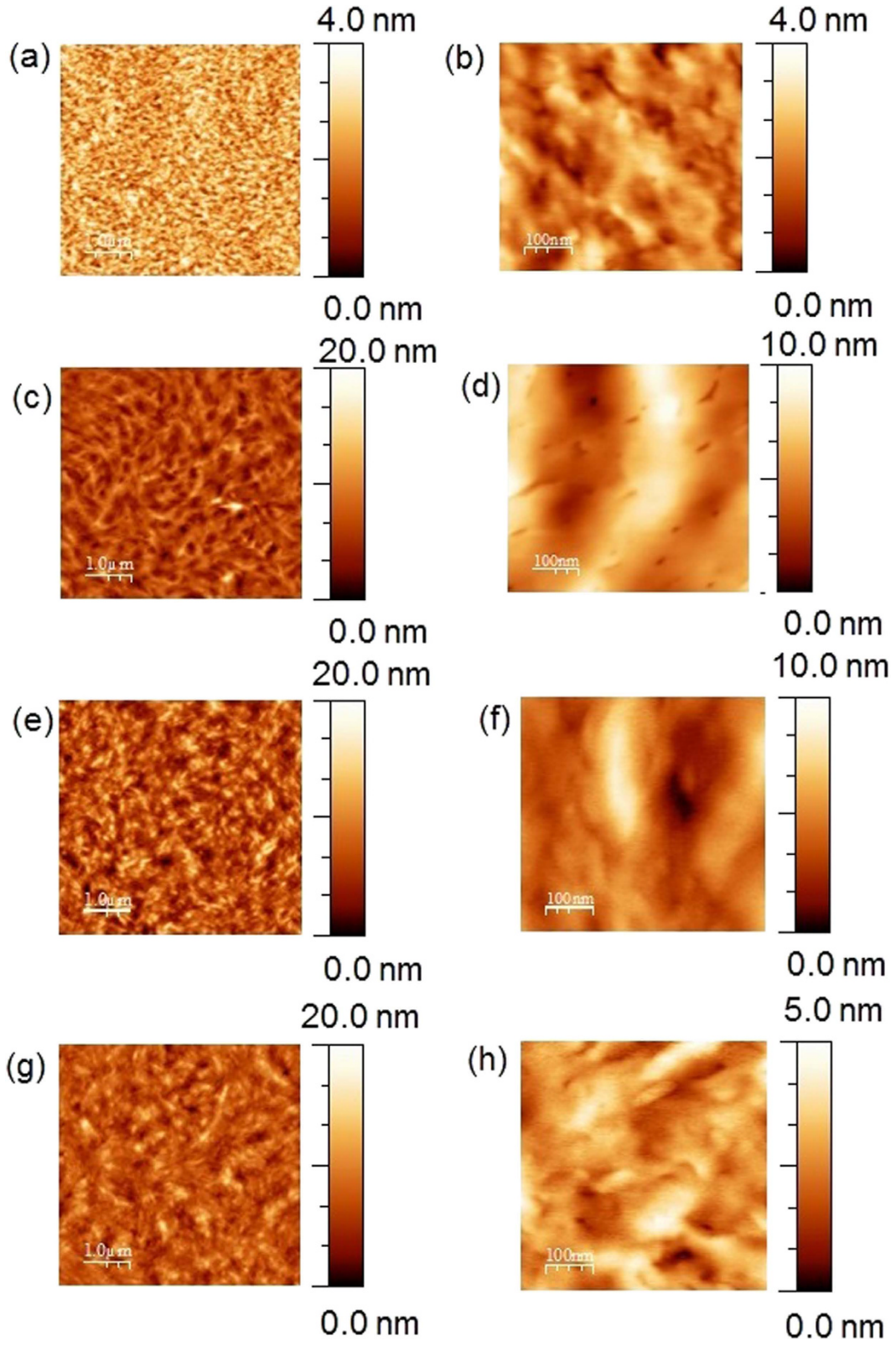

Figure 1. (Left) Atomic force microscopy (AFM) images of the p-DTS(FBTTh2)2:PC71BM films (**a**) as prepared (**c**)thermally annealed at 100 °C. (**e**) with 0.25 vol% DIO (**g**) with 0.25 vol% DIO thermally annealed at 80 °C (Right) High resolution images of *p*-DTS(FBTTh$_2$)$_2$:PC$_{71}$BM films.

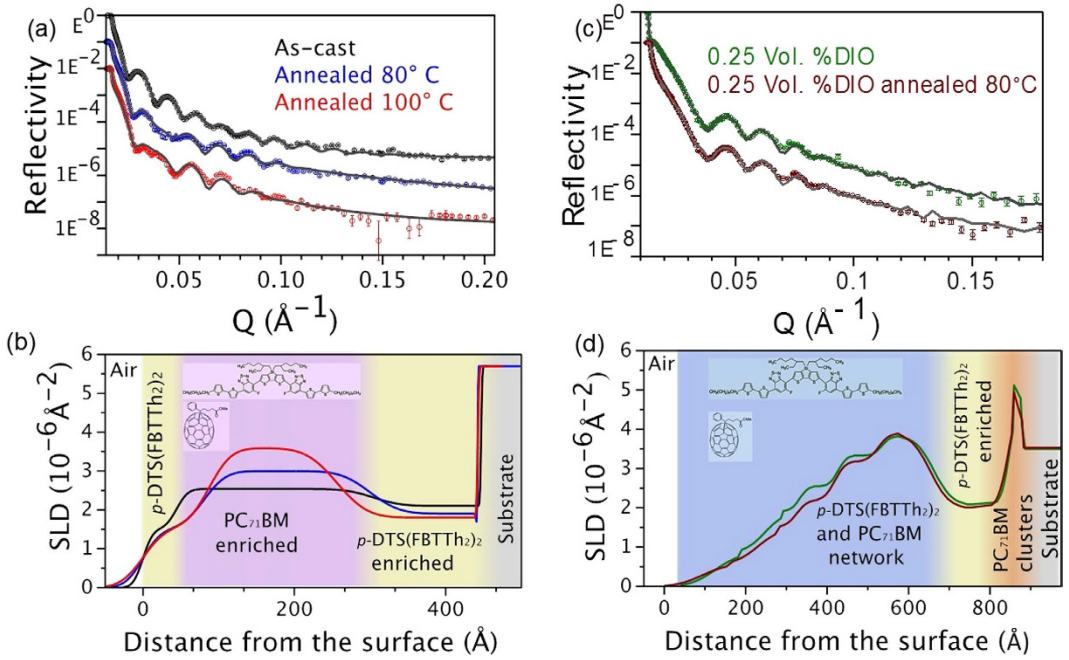

Figure 2. (**a**) Neutron reflectivity data of Al_2O_3*p*-DTS(FBTTh$_2$)$_2$:$PC_{71}BM$ BHJ test structures as prepared and annealed at 80 °C, 100 °C. Experimental data are shown as symbols and the fits as lines. (**b**) Scattering length density (SLD) profiles as a function of distance from the surface obtained after the fits to the experimental NR data of Fig 1(a). (**c**) Neutron reflectivity data of SiO_2*p*-DTS(FBTTh$_2$)$_2$:$PC_{71}BM$ BHJ with 0.25 V% DIO device as prepared and annealed at 80 °C. Experimental data are shown as symbols and the fits as lines. (**d**) Scattering length density (SLD) profiles as a function of distance from the surface from fitting the experimental NR data of (**c**).

phase morphology of the OPV devices. Figure 2(a) presents neutron reflectivity (NR) for as-cast, and thermally annealed films at 80 °C and 100 °C as a function of out-of-plane momentum transfer, Q_z of specular reflections. Here, $Q_z = (4\pi/\lambda)\sin\alpha_i$ with λ and α_i being the wavelength and the incident angle of neutron beam, respectively. The associated fit of the data obtained based on Parratt recursion formalism is shown as solid line[46]. We estimated the value of neutron scattering length density (*n*SLD) for *p*-DTS(FBTTh$_2$)$_2$ to be 1.33×10^{-6} Å^{-2} (see experimental methods). The *n*SLD value of $PC_{71}BM$ was found to be 4.34×10^{-6} Å^{-2} based on the bulk density of 1.5 g/cm^3 of PCBM and neutron scattering lengths of the constituent elements[37]. Figure 2(b) shows the *n*SLD profiles of the best fit to the reflectivity data. A detailed description of models used to fit the data is given in the Supplementary Materials (Fig. S3). From the fits, the total thickness of the as-cast film was found to be ~45 nm. The *n*SLD profiles in Fig. 2(b) reveal three distinct layers with the composition characterized by different *n*SLDs: 1) top surface layer in contact with the air/film interface, 2) a bottom layer interfacing with the substrate, and 3) a bulk layer sandwiched by the two interfacial layers. It also shows that the *n*SLD of the sandwiched layer increases with annealing temperature while that of the bottom layer decreases. The changes in *n*SLDs of the bulk and bottom layer are associated with the inter-diffusion of *p*-DTS(FBTTh$_2$)$_2$ and $PC_{71}BM$. Remarkably, the *n*SLD of top interfacial layer remained almost unchanged regardless of thermal annealing. These results indicate that *p*-DTS(FBTTh$_2$)$_2$ prefers the two interfacial regions, whereas $PC_{71}BM$ tends to diffuse to the bulk layer. To complement the depth phase morphology deduced by NR data fits, we performed X-ray reflectivity measurements shown in Fig. S4. Although the contrast between X-ray SLDs (*x*SLDs) of *p*-DTS(FBTTh$_2$)$_2$ and $PC_{71}BM$ is relatively low as compared to *n*SLDs, we observed an obvious change in *x*SLD with thermal annealing. The total number of sub-layers and the thermally induced changes such as enhancement of *x*SLD in the bulk layer and reduction in the film thickness are consistent with the NR results.

Figure 2(c) shows the neutron reflectivity profiles of as-cast and annealed *p*-DTS(FBTTh$_2$)$_2$:$PC_{71}BM$ films prepared using 0.25 vol.% DIO. From the NR fits, the *n*SLD profiles were extracted and are depicted in Fig. 2(d). The *n*SLD profile of the as-cast film with 0.25 vol.% DIO is remarkably different from the one without additive. Although it shows the presence of *p*-DTS(FBTTh$_2$)$_2$ enriched bottom interfacial layer, its width is about 3 to 4 times thinner than in the samples without DIO. Further, a thermal annealing the film with DIO at 80 °C induces only small change in the *n*SLD profile. This is different from the change in *n*SLD profile for as-cast *p*-DTS(FBTTh$_2$)$_2$:$PC_{71}BM$ film and sample annealed at 80 °C (Fig. 2(b)). It indicates that no significant inter-diffusion of *p*-DTS(FBTTh$_2$)$_2$ and $PC_{71}BM$ occurs by the thermal annealing. This observation is consistent with our AFM data where the films show densely packed structure

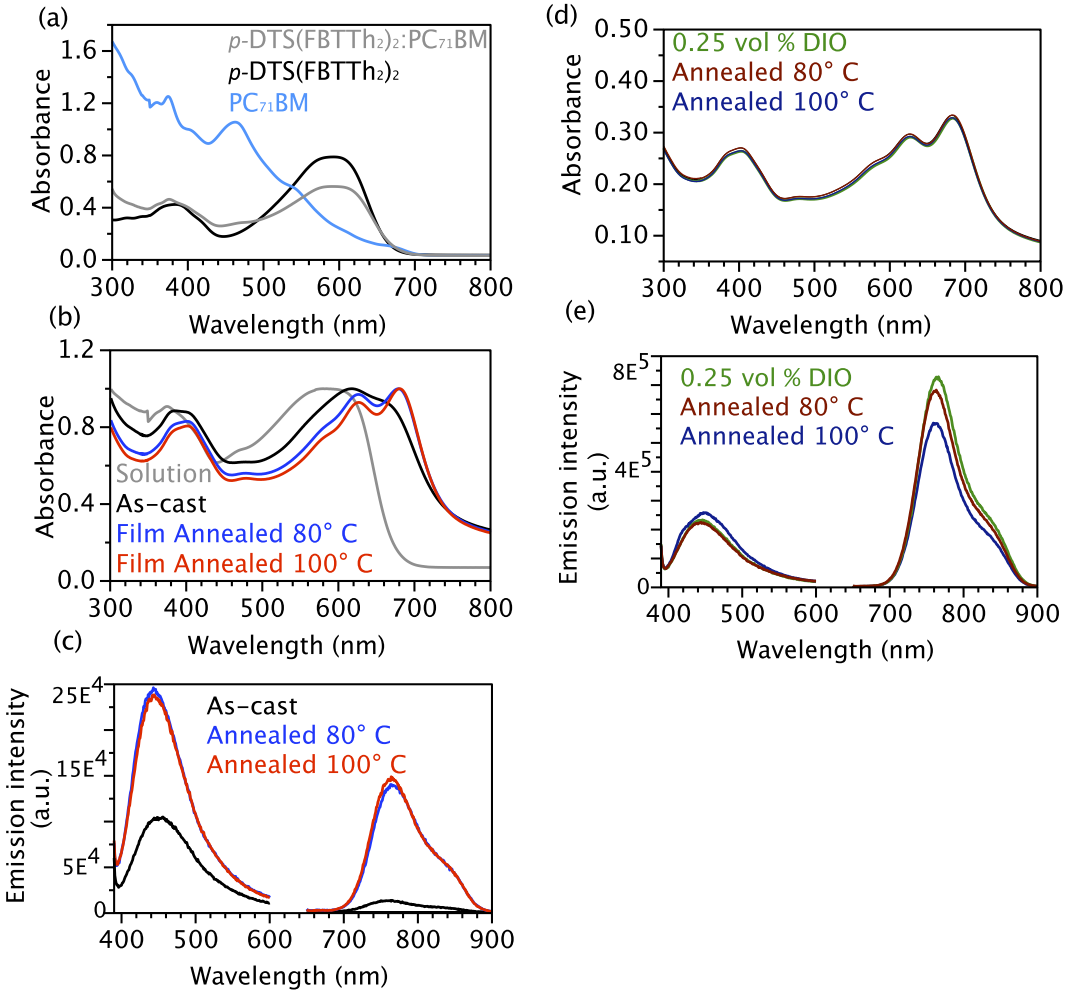

Figure 3. (**a**) UV-Visible absorption spectra of *p*-DTS(FBTTh$_2$)$_2$, PC$_{71}$BM and blend of *p*-DTS(FBTTh$_2$)$_2$:PC$_{71}$BM in chlorobenzene solvent (**b**) Absorption spectra of *p*-DTS(FBTTh$_2$)$_2$:PC$_{71}$BM blend solution and cast films under thermal annealing. The absorption intensities are normalized. (**c**) Photoluminescence spectra of as-cast *p*-DTS(FBTTh$_2$)$_2$:PC$_{71}$BM film after thermal annealing at 80 °C and 100 °C. (**d**) UV- Visible absorption and (**e**) photoluminescence spectra of *p*-DTS(FBTTh$_2$)$_2$:PC$_{71}$BM with 0.25 vol.% DIO after thermal annealing at 80 °C.

with reduced surface roughness. Furthermore, at the bottom substrate/film interfaces, NR revealed a ~20 nm thick layer with a high *n*SLD value of ~6×10^{-6} Å^{-2} in both as-cast and annealed samples with DIO. The peaks correspond to high-density PC$_{71}$BM clusters formed in the samples with DIO[47]. Upon thermal annealing, the *n*SLD of the profile increased resulting densely packed films.

These results show that presence of DIO results in much more evolved film morphology, which is close to the equilibrium state than that of the film spun-cast without DIO. Hence, thermal annealing only results in small refinement in the structure with negligible difference from as spun-cast film[45]. It is evident from the *n*SLD profiles that, for as-cast samples, accumulation of the ED material at the air/film interface was enhanced with thermal annealing, which was previously observed using X-ray photon spectroscopy (XPS) for *p*-DTS(FBTTh$_2$)$_2$ material[11]. By contrast, polymer: fullerene blend systems exhibit accumulation of PCBM (PC$_{61}$BM or PC$_{71}$BM) at film/substrate and air/film interfaces which is believed to be responsible for enhanced electron extraction[38,39]. Hence, the layer morphology of *p*-DTS(FBTTh$_2$)$_2$:PC$_{71}$BM appears very differently from polymer: fullerene blend systems.

The structural evolution of SM in solutions and films can be correlated with the changes in electronic and photoluminescence spectra. We assigned the broad absorption peaks at 390 and 600 nm in chlorobenzene (CB) solutions of *p*-DTS(FBTTh$_2$)$_2$, PC$_{71}$BM to π–π* transition of *p*-DTS(FBTTh$_2$)$_2$, while 370 nm and 460 nm peaks were ascribed to the PC$_{71}$BM, Fig. 3(a). Upon spin casting of the *p*-DTS(FBTTh$_2$)$_2$:PC$_{71}$BM solution into film, a bathochromic shift of all absorption peaks is observed. As-cast thin film exhibits 550, 615 and 680 nm broad vibronic peaks of π–π stacked *p*-DTS(FBTTh$_2$)$_2$ aggregates, assigned to $A_{0\rightarrow2}$, $A_{0\rightarrow1}$ and $A_{0\rightarrow0}$ transitions respectively[48]. The ratio of $A_{0\rightarrow1}/A_{0\rightarrow0} > 1$ is indicative of

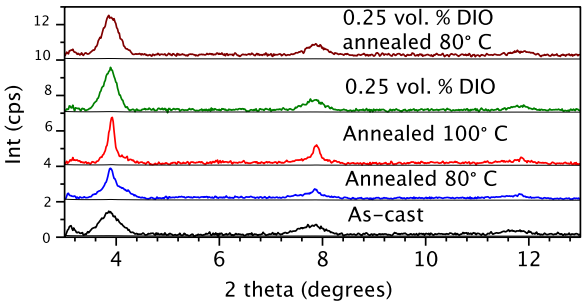

Figure 4. Out of plane X-ray diffraction scans of *p*-DTS(FBTTh$_2$)$_2$:PC$_{71}$BM blends. $2\theta = 3.98°$, 7.88° and 11.90°. With thermal annealing, the intensity of the peaks is enhanced. Addition of 0.25 vol% DIO generated broader peak with higher intensities.

Sample	Normalized Peak Area	Crystallite size (nm)
As cast	2205	22.8
Annealed at 80 °C	2358	41.2
Annealed at 100 °C	3189	134.7
With 0.25 V% DIO	6687	24.6
With 0.25 V% DIO ann. 80 °C	7386	26.4

Table 1. Peak area and the crystallite sizes for *p*-DTS(FBTTh$_2$)$_2$ (001) reflection.

dominating inter-chain coupling in π−π stacked *p*-DTS(FBTTh$_2$)$_2$ aggregates[48]. Upon thermal annealing at 80 °C and 100 °C, the $A_{0\to2}$, $A_{0\to1}$ and $A_{0\to0}$, vibronic peaks become more pronounced and show small bathochromic shift, indicative of an enhanced crystalline ordering in SM aggregates. The reduced intensity ratio of $A_{0\to1}/A_{0\to0} < 1$ is usually attributed to planarization of *p*-DTS(FBTTh$_2$)$_2$ molecules, with intra-chain interactions dominating over inter-chain coupling in SM aggregates. The PL spectra of the DTS(FBTTh$_2$)$_2$:PC$_{71}$BM film show two broad emission bands with maxima at 460 nm (2.7 eV) and 765 nm (1.6 eV), when excited at 320 nm and 580 nm, respectively. The 1.6 eV emission correlates with the transition between LUMO and HOMO of *p*-DTS(FBTTh$_2$)$_2$ aggregates, while the 2.7 eV band was assigned to the transition from $LUMO_{p\text{-DTS(FBTTh2)2}}$ to $HOMO_{PC71BM}$[25]. Annealing leads to increased PL intensity of 1.6 eV and 2.7 eV peaks, which correlates well with the changes in absorption spectra, and is probably related to the increase in *p*-DTS(FBTTh$_2$)$_2$ aggregate π−π stacking and the structure of *p*-DTS(FBTTh$_2$)-PC$_{71}$BM interface respectively.

The absorption spectra of as-cast and annealed *p*-DTS(FBTTh$_2$)$_2$:PC$_{71}$BM films are shown in Fig. 3(d). In addition to a broad ~400 nm peak, a progression of vibronic peaks was detected at 580 nm, 625 nm, and 680 nm, which are assigned to $A_{0\to2}$, $A_{0\to1}$, and $A_{0\to0}$ transitions, respectively. The ratio of $A_{0\to1}$ to $A_{0\to0}$ peak intensities was found to be less than one which does not change upon annealing, indicating that high order of π−π stacking and molecular planarization in SM aggregate in the presence of DIO are achieved already at room temperature. PL spectra show same peaks without DIO. However, while the intensity of broad 2.7 eV peak did not change, the intensity of low energy emission peak at 1.6 eV increased by a factor of five compared to annealed *p*-DTS(FBTTh$_2$)$_2$:PC$_{71}$BM films without DIO. The improved PL intensity indicates that defect-related non-radiative transition is suppressed in the case of DIO containing films, due to better ordering of SM aggregates. Both electronic absorption and PL spectra of annealed DIO containing *p*-DTS(FBTTh$_2$)$_2$:PC$_{71}$BM films show that thermodynamically metastable molecular ordering was achieved already at room temperature. This metastable molecular ordering is consistent with the unchanged vertical phase morphology of DIO containing *p*-DTS(FBTTh$_2$)$_2$:PC$_{71}$BM films observed in NR experiments.

To gain insights into the effect of DIO and thermal annealing on the molecular packing and crystallinity of *p*-DTS(FBTTh$_2$)$_2$:PC$_{71}$BM films, we conducted X-ray diffraction (XRD) measurements. Figure 4 shows XRD patterns for as-cast and annealed films with and without DIO. All films exhibit a peak at $2\theta = \sim3.90°$, which is associated with the (001) reflection of *p*-DTS(FBTTh$_2$)$_2$ crystal. Higher order (002) and (003) reflections observed at ~7.88°, and ~11.74° manifests that a fraction of *p*-DTS(FBTTh$_2$)$_2$ chains are highly-ordered aggregates within films[14]. Upon annealing of thin films, the XRD peak intensity and sharpness increase, indicating an increase in ordering of *p*-DTS(FBTTh$_2$)$_2$ aggregates. Using the Scherrer equation, the size of crystalline domain of SM aggregate was calculated along with the peak areas for

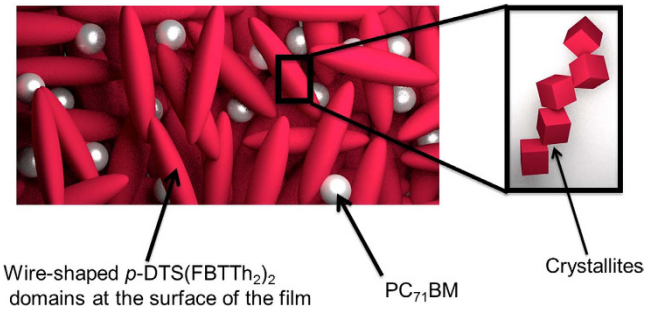

Figure 5. Schematic illustration of the change of surface morphology with addition of DIO. With 0.25 vol% DIO, *p*-DTS(FTTh$_2$)$_2$ shows to generate ~200 nm long wire-shaped domains structures, which are made up of ~26 nm crystallites. This illustration is drafted using data obtained from AFM, neutron reflectometry and XRD measurements.

(001) reflection of *p*-DTS(FBTTh$_2$)$_2$ crystal (Table 1). The crystalline domain size in as-cast films were found to be ~22.8 nm, which increases to 41.2 nm and 134.7 nm after thermal annealing at 80 °C and 100 °C, respectively. The integrated (001) peak area of the sample annealed at 100 °C is greater than that of the as-cast sample, suggesting an increased population of crystalline domains of *p*-DTS(FBTTh$_2$)$_2$ in the annealed *p*-DTS(FBTTh$_2$)$_2$:PC$_{71}$BM film (Table 1). Remarkably the integrated area of (001) peak of as-cast *p*-DTS(FBTTh$_2$)$_2$:PC$_{71}$BM films with DIO is about three times larger than that without DIO. Interestingly, the crystalline domain size of sample is ~24.6 nm, which is a ~2 nm increase to that of film without DIO. We conclude that DIO drastically increases the population of *p*-DTS(FBTTh$_2$)$_2$ crystal domains already in as-cast films, and only slightly increases the crystal domain size. Thermal annealing of DIO-containing *p*-DTS(FBTTh$_2$)$_2$:PC$_{71}$BM films increases the size and the population of *p*-DTS(FBTTh$_2$)$_2$ crystalline domains. We also observe that the size of crystalline domains in annealed (80 °C) DIO-containing *p*-DTS(FBTTh$_2$)$_2$:PC$_{71}$BM films is smaller by a factor of 1.6 compared to that in annealed *p*-DTS(FBTTh$_2$)$_2$:PC$_{71}$BM films without DIO while the population of crystals increases by a factor of 3. Larger crystal domain size in annealed *p*-DTS(FBTTh$_2$)$_2$:PC$_{71}$BM films suggests that excitons have to travel longer distances to reach D/A interface, which is detrimental for achieving high PCEs.

Combining results of AFM, XRD and neutron reflectometry allows visualization of the surface and depth morphology of *p*-DTS(FBTTh$_2$)$_2$:PC$_{71}$BM thin films, which is shown in Fig. 5. The drawing shows changes in the blend microstructure upon thermal annealing and addition of DIO. Formation of wire-shaped domains in the films generated uneven surfaces, with the roughness of ~20 nm. Our NR data reveals that surface of films consist of *p*-DTS(FBTTh$_2$)$_2$ and PC$_{71}$BM. These wire-shaped features can be attributed to *p*-DTS(FBTTh$_2$)$_2$ domians[13]. In addition, the lengths of the wires are much longer than the crystallite sizes obtained from our XRD. This could be due to the fact that these wires are made of few crystallites connected together through $\pi-\pi$ stacking.

Figure 6 shows the current density versus voltage (*J*-*V*) curves of *p*-DTS(FBTTh$_2$)$_2$:PC$_{71}$BM solar cells under AM 1.5 G, 100 mW/cm^2 irradiation from a solar simulator. The photovoltaic parameters such as short circuit current density (J_{SC}), open circuit voltage (V_{OC}), fill factor (FF) and power conversion efficiency (PCE) are listed in Table 2, based on the statistical average of ten devices. The device consisting of *p*-DTS(FBTTh$_2$)$_2$:PC$_{71}$BM active layer shows relatively low value of PCE, about 2.04%. After thermal annealing, the PCE increases to 3.18% at 80 °C and 3.48% at 100 °C. DIO-containing DTS(FBTTh$_2$)$_2$:PC$_{71}$BM devices show higher performance with PCE of 4.95% for as-cast active layer, which increases to 5.27% after annealing at 80 °C. The improved performance of DIO-containing device results for the fact that the additive induces crystallization of size of SM aggregates with better spectral response as indicated by increase in PL[49].

To model the effect of annealing and of DIO additive on the phase separation in SM OPV system, we have constructed a phase diagram for the four-component system (*p*-DTS(FBTTh$_2$)$_2$:PCBM:CB:DIO) using Flory-Huggins theory,[50] corroborated by large-scale molecular dynamics simulations[45,51]. Structural parameters for molecules used in the theory are shown in Table S1. Values of Flory's χ_{ij} are summarized in Table 3, with the higher value indicating stronger repulsive interactions between *i* and *j* components. The quarternary phase diagram computed using the Flory-Huggins theory for the *p*-DTS(FBTTh$_2$)$_2$:PC$_{71}$BM:CB:DIO system is shown in Fig. 7. The phase diagram highlights the different thermodynamic pathways to reach the same binary blend of *p*-DTS(FBTTh$_2$)$_2$ and PC$_{71}$BM. One path is along the CB-PC$_{71}$BM- *p*-DTS(FBTTh$_2$)$_2$ plane in Fig. 7, where movement towards the binary blend state point is driven by solvent (i.e., CB) evaporation. Treating *p*-DTS(FBTTh$_2$)$_2$ and PC$_{71}$BM as oligomers with the degree of polymerization of 10 and 6, respectively, to account for disparity in molar volume with respect to the solvent CB (cf. Table S1) phase diagram can be readily constructed using the Flory-Huggins theory exhibiting a critical point at $\phi_{p\text{-DTS(FBTTh2)2}} = 0.44$ and $\chi_{DTS,PCBM} = 0.26$. The experimental system in this work contains 21 mg/ml of *p*-DTS(FBTTh$_2$)$_2$ mixed with 14 mg/ml of PC$_{71}$BM, corresponding to a

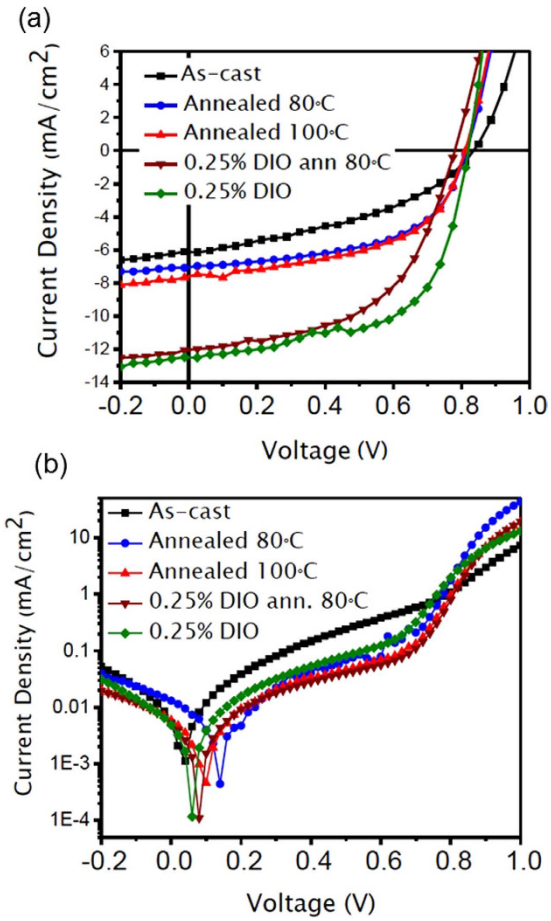

Figure 6. J-V characteristics of the p-DTS(FBTTh2)2:PC71BM BHJ solar cells at different processing conditions (**a**) under AM 1.5 G irradiation at 100 mW/cm^2 (**b**) in the dark.

Device	J_{SCavg} (mA/cm^2)	V_{OCavg} (V)	FF_{avg} (%)	PCE_{avg} (%)
As cast	6.66	0.81	37.84	2.04 ± 0.29
Annealed at 80 °C	7.62	0.81	51.40	3.18 ± 0.30
Annealed at 100 °C	7.85	0.81	54.60	3.48 ± 0.32
With 0.25 V% DIO	11.74	0.78	54.24	4.95 ± 0.07
With 0.25 V% DIO ann. 80 °C	12.01	0.76	58.15	5.27 ± 0.48

Table 2. Electrical Parameters of *p*-DTS(FBTTh$_2$)$_2$:PC$_{70}$BM solar cells at different processing conditions. Values are obtained from averaging parameters from ten devices.

Parameter	i = p-DTS, j = $PC_{71}BM$	i = DTS, j = CB	i = DTS, j = DIO	i = $PC_{71}BM$, j = CB	i = $PC_{71}BM$, j = DIO	i = CB, j = DIO
χ_{ij}	0.34 + 13.19/T (0.384)	0.34 + 90.64/T (0.644)	0.34 + 436.37/T (1.804)	0.34 + 108.44/T (0.703)	0.34 + 431.65/T (1.788)	0.34 + 29.50/T (0.439)

Table 3. Estimated χ_{ij} for different pairs along with their values (in parenthesis) at T = 298 K, relevant for this study.

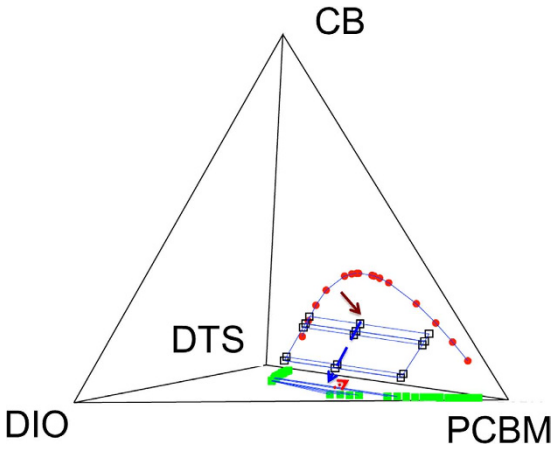

Figure 7. Phase diagram for the *p*-DTS(FBTTh$_2$)$_2$:PC$_{71}$BM:CB:DIO system constructed using the Flory-Huggins theory showing different thermodynamic pathways in the presence and absence of DIO. In this figure, the label DTS represents *p*-DTS(FBTTh$_2$)$_2$ and the blue lines represent the tie lines.

volume fraction of *p*-DTS(FBTTh$_2$)$_2$ equal to $\phi_{p\text{-DTS(FBTTh2)2}} = 0.60$. An estimated value of $\chi_{DTS,PCBM} = 0.38$ at room temperature using the group contribution method, segregation between *p*-DTS(FBTTh$_2$)$_2$ and PC$_{71}$BM can be expected in the experimental *p*-DTS(FBTTh$_2$)$_2$:PC$_{71}$BM mixture towards equilibrium binary phases. It agrees with the NR observation that *p*-DTS(FBTTh$_2$)$_2$ and PC$_{71}$BM distribute heterogeneously along vertical direction of *p*-DTS(FBTTh$_2$)$_2$:PC$_{71}$BM film annealed at different temperatures. For instance, the volume fractions of *p*-DTS(FBTTh$_2$)$_2$ in film annealed at 100 °C shows $\phi_{p\text{-DTS(FBTTh2)2}} = 0.8$, 0.4 and 0.7 in surface, bulk and substrate layers, respectively. Given the simplistic nature of the Flory-Huggins theory, such a qualitative agreement with the experiments is quite remarkable.

Conversely, DIO-containing *p*-DTS(FBTTh$_2$)$_2$:PC$_{71}$BM films show slight change in crystal domain size after thermal annealing, which is probably due to the change in miscibility of PC$_{71}$BM in chlorobenzene after adding DIO. The miscibility of PC$_{71}$BM is higher in the presence of DIO additives[15]. In this case, *p*-DTS(FBTTh$_2$)$_2$ might crystallize resulting in smaller but highly populated crystal growth. As the boiling point of DIO is much higher than CB, DIO could remain in a spun-cast film even after complete evaporation of CB. During spin coating, the DIO additive facilitates the formation of well-ordered structure, with donor and acceptor materials forming nano-scale domains, favorable for efficient charge transport. NR reveals the formation of a thin layer of PC$_{71}$BM clusters at the film/substrate interface with addition of DIO. A 3-D tomography study conducted by Li *et al.* observed similar vertical elongated clusters for polymer, HXS-1 and PCBM based solar cells with 2.5 vol.% DIO[47]. According to their study, these clusters facilitate the charge transport and minimize the charge recombination of the devices. NR also reveals the formation of a *p*-DTS(FBTTh$_2$)$_2$ rich layer at the surface without DIO, without reduction of charge carrier mobility. This can be explained in terms of increased phase purity as evident by NR and XRD data, which facilitates the efficient charge transport through the devices observation and agrees well with previously published results[34]. Notably, the addition of DIO improves OPV performances, namely, changing value of FF from 38.84% to 58.15%,and the value of J_{SC} from 6.66 to 12.01, and leading to larger value of PCE = 5.27%.

Flory-Huggins theory also shed light on the effects of DIO additive with *p*-DTS(FBTTh$_2$)$_2$ and PC$_{71}$BM blends. In the presence of DIO, which is less volatile than the parent solvent (CB), evaporation of the additive leads to the second path along a direction out-of-plane due to further evaporation of DIO until the system runs out of the parent solvent completely. Complete evaporation of the additive brings DIO- *p*-DTS(FBTTh$_2$)$_2$:PC$_{71}$BM plane to the final blend of *p*-DTS(FBTTh$_2$)$_2$:PC$_{71}$BM. These thermodynamic calculations highlight that although the nature of the final stage is the same, independent of the presence or absence of solvent additives, the kinetic processes (such as evaporation rates, mobility of *p*-DTS(FBTTh$_2$)$_2$ and PC$_{71}$BM) are important to differentiate between the morphological differences. For example, Table 3 reveals that both the CB and DIO are non-selective solvents for the *p*-DTS(FBTTh$_2$)$_2$ and PC$_{71}$BM (i.e. $\chi_{DTS,CB} = \chi_{PCBM,CB}$, $\chi_{DTS,DIO} = \chi_{PCBM,DIO}$) suggesting that the CB as well as DIO will stabilize interfaces between *p*-DTS(FBTTh$_2$)$_2$ and PC$_{71}$BM domains due to entropic effects. However, $\chi_{DTS,CB}$ is less than $\chi_{DTS,DIO}$ suggesting that DIO results in better entropic stabilization of interfaces. The latter is in qualitative agreement with the X-ray diffraction analysis, which shows that DIO increases population of smaller crystalline domain size of *p*-DTS(FBTTh$_2$)$_2$ aggregates in *p*-DTS(FBTTh$_2$)$_2$:PC$_{71}$BM films. In this study, we have developed and proposed a strategy by combining experimental and theoretical approach. This approach allows us to demonstrate the correlation between the morphology and device performances as well as the origin of different morphologies. Such information may aid in improving the morphology and to enhance the device performance for OPV devices.

Conclusions

We report that the thermodynamically stable *p*-DTS(FBTTh$_2$)$_2$:PC$_{71}$BM BHJs obtained by thermal annealing are different in lateral and depth phase morphology and crystallinity from BHJs obtained with a DIO additive. Through an energy-level analysis on the absorption and emission spectra of the films, the different functions of thermal or DIO treatment to the $\pi-\pi$ stacking in *p*-DTS(FBTTh$_2$) aggregates and the interaction at *p*-DTS(FBTTh$_2$)$_2$-PC$_{71}$BM interface have also been revealed. The three-layer vertical phase morphology was observed for the films after thermal annealing. By contrast, DIO additive processing generates more evolved film morphology, which is closer to the equilibrium state. *n*SLD chemical/structural profiles obtained from NR data show more densely packed structures, which are consistent with the AFM images. Formation of well-mixed ED and EA regions at the surface of the film facilitates the efficient charge transfer to the device. According to X-ray diffraction data, the DIO additive morphology exhibits a high density of small donor nanocrystallites of ~24 nm, whereas thermal annealing generates smaller amount of much larger crystallites (~134 nm). DIO promotes the formation of a large density of *p*-DTS(FBTTh$_2$)$_2$ small nanocrystals arranged in an elongated network throughout the thickness of the active layer, and it results in the enhancements of solar cell performance due to the formation of nanocrystallites with the domain size comparable to the maximum exciton diffusion length. This is favorable for device efficiencies, since they stimulate efficient exciton diffusion (less probable to recombine) to an ED/EA interface and provide a larger ED/EA interfacial area for exciton dissociation. Thermodynamic analysis based on the Flory-Huggins theory for the experimentally studied systems reveals that the CB as well as DIO act as non-selective solvents for the *p*-DTS(FBTTh$_2$)$_2$:PC$_{71}$BM blends (i.e., $\chi_{DTS,CB}=\chi_{PCBM,CB}$, $\chi_{DTS,DIO}=\chi_{PCBM,DIO}$). However, DIO has an increased tendency to induce phase segregation resulting from the fact that $\chi_{DTS,CB}<\chi_{DTS,DIO}$. Furthermore, the inverse temperature dependence of the χ parameters allows us to infer the effects of temperature on the phase segregation, which is in qualitative agreement with the observed morphological changes. Our findings demonstrate the role and impact of DIO and thermal treatment on the morphology of small molecule BHJ and take us a step closer to fully controlling the performance of photovoltaic devices.

Methods

Devices fabrication. *p*-DTS(FBTTh$_2$)$_2$ and PC$_{71}$BM were purchased from "1-Material". The blends of *p*-DTS(FBTTh$_2$)$_2$ (21 mg) and PC$_{71}$BM (14 mg) were dissolved in chlorobenzene (1 ml) with and without 0.25 Vol.% diiodooctane. Solutions were heated at 60 °C for several hrs and 90 °C for 15 min just before spin casting. Devices were fabricated as follows: ITO substrates were first cleaned by detergent and subsequently sonicated in DI water, acetone, and isopropyl alcohol (IPA), followed by backing at 100 °C for an hr. The cleaned ITO substrates were then treated with UV Ozone for 20 min, and PEDOT:PSS solution was spun-cast on them and baked for 1 hour at 135 °C in air. The blend solutions with and without DIO were spun-cast on the PEDOT:PSS-coated substrates at a spinning speed of 2000 rpm for 45 s. Films were allowed to dry for 20 min under inert atmosphere and annealed at 80 °C for 10 min. Devices without DIO were annealed at either 80° or 100 °C for 10 min. Finally, Ca and Al electrodes were deposited on top of the active layers through a shadow mask by the thermal evaporation. The electrode area of the cells was 22.6 mm^2. The J-V characteristics of the prepared devices were measured by a Keithley 4200 semiconductor parameter analyzer under the AM 1.5 conditions (100 mW/cm^2).

The morphological characterizations were done with blends of *p*-DTS(FBTTh$_2$)$_2$:PC$_{71}$BM BHJ spun cast on sapphire (Al_2O_3) or quartz (SiO_2) substrates. To obtain the neutron scattering density (nSLD) of pure *p*-DTS(FBTTh$_2$)$_2$, a solution of *p*-DTS(FBTTh$_2$)$_2$ (12 mg/ml) in chlorobenzene was prepared and spun-cast onto a silicon wafer.

Thin film characterizations

Neutron reflectomety. The neutron reflectometry experiments were performed at the Magnetism Reflectometer (BL 4A) and the Liquid Reflectometer (BL 4B) at the Spallation Neutron Source at Oak Ridge National Laboratory. The data were recorded on position sensitive detectors and the reflected and scattered intensity signals were normalized to the intensity spectrum of the incident beam. The data are presented in two-dimensional maps as a function of p_i and p_f where $p_i=2\pi\ \sin\alpha_i/\lambda$ and $p_f=2\pi\ \sin\alpha_j/\lambda$ are the perpendicular components of the neutron wave vectors. The specular reflectivities are extracted from these two-dimensional intensity maps as a function of incident momentum transfer normal to the surface, $Q_z=p_i+p_j=4\pi\ \sin\alpha_i/\lambda$. The experiential data is used to extract neutron scattering length density (*n*SLD) values.

X-ray Diffraction and X-ray reflectomety. Measurements were carried out on a high-resolution PANalytical X'Pert Pro MPD diffractometer with a Cu Kα source (wavelength 1.5405 Å). The X-ray diffraction measurements were performed at 2.5–35 Å angular range with 0.04° step size and 0.5° scan speed. Standard single crystal silicon single crystal sample was used measured to calibrate the instrument.

UV-Visible absorption and PL measurements. UV-Vis absorption spectra (Abs) were recorded using a Cary 5000 spectrometer from the film obtained by solution spin-casting and subsequent thermal processing. Photoluminescence (PL) was measured using a FluoroLog 3 T fluorescence spectrometer, the excitation monochromator was set at 320 nm and 580 nm.

AFM. Atomic Force microscopy was recorded using Bruker Dimension Icon operating in a tapping mode.

References

1. Hoppe, H. & Sariciftci, N. S. Organic solar cells: An overview. *J. Mater. Res.* **19,** 1924–1945, doi: 10.1557/jmr.2004.0252 (2004).
2. Darling, S. B. & You, F. The case for organic photovoltaics. *RSC Advances* **3,** 17633–17648, doi: 10.1039/C3RA42989J (2013).
3. Yu, G., Gao, J., Hummelen, J. C., Wudl, F. & Heeger, A. J. Polmer photovoltaics cells- enhances efficiencies via a network of internal donor-acceptor heterojunctions *Science* **270,** 1789–1791, doi: 10.1126/science.270.5243.1789 (1995).
4. Coropceanu, V. *et al.* Charge transport in organic semiconductors. *Chem. Rev.* **107,** 926–952, doi: 10.1021/cr050140x (2007).
5. Brabec, C. J. *et al.* Polymer-fullerene bulk-heterojunction solar cells. *Adv. Mater.* **22,** 3839–3856 (2010).
6. Ma, W., Yang, C., Gong, Lee, K. & Heeger, A. J. Thermally stable, efficient polymer solar cells with nanoscale control of the interpenetrating network morphology. *Adv. Funct. Mater.* **15,** 1617–1622 (2005).
7. Xu, Z., Wu, Y., Hu, B., Ivanov, I. N. & Geohegan, D. Carbon nanotube effects on electroluminescence and photovoltaic response in conjugated polymers. *Phys. Lett* **87,** 263118 (2005).
8. Peet, J., Heeger, A. J. & Bazan, G. C. "Plastic" Solar Cells: Self-Assembly of Bulk Heterojunction Nanomaterials by Spontaneous Phase Separation. *Acc. Chem. Resea.* **42,** 1700–1708, doi: 10.1021/ar900065j (2009).
9. Cheun, H. *et al.* Roles of thermally-induced vertical phase segregation and crystallization on the photovoltaic performance of bulk heterojunction inverted polymer solar cells. *Ener. Environ. Sci.* **4,** 3456–3460, doi: 10.1039/c1ee01316e (2011).
10. He, M. *et al.* Annealing effects on the photovoltaic performance of all-conjugated poly(3-alkylthiophene) diblock copolymer-based bulk heterojunction solar cells. *Nanoscale* **3,** 3159–3163, doi: 10.1039/c1nr10293a (2011).
11. Leong, W. L. *et al.* Understanding the Role of Thermal Processing in High Performance Solution Processed Small Molecule Bulk Heterojunction Solar Cells. *Adv. Ener. Mater.* **3,** 356–363, doi: 10.1002/aenm.201200631 (2013).
12. Ruderer, M. A. & Muller-Buschbaum, P. Morphology of polymer-based bulk heterojunction films for organic photovoltaics. *Soft Matt.* **7,** 5482–5493, doi: 10.1039/c0sm01502d (2011).
13. Love, J. A. *et al.* Film Morphology of High Efficiency Solution-Processed Small-Molecule Solar Cells. *Adv. Funct. Mater.* **23,** 5019–5026, doi: 10.1002/adfm.201300099 (2013).
14. Perez, L. A. *et al.* Solvent Additive Effects on Small Molecule Crystallization in Bulk Heterojunction Solar Cells Probed During Spin Casting. *Adv. Mater.* **25,** 6380 (2013).
15. Liao, H.-C. *et al.* Additives for morphology control in high-efficiency organic solar cells. *Mater. Today* **16,** 326–336, doi: dx.doi.org/10.1016/j.mattod.2013.08.013 (2013).
16. Yang, X. & Loos, J. Toward high-performance polymer solar cells: The importance of morphology control. *Macromolecules* **40,** 1353–1362, doi: 10.1021/ma0618732 (2007).
17. Rivnay, J. *et al.* Drastic Control of Texture in a High Performance n-Type Polymeric Semiconductor and Implications for Charge Transport. *Macromolecules* **44,** 5246–5255, doi: 10.1021/ma200864s (2011).
18. Mikhnenko, O. V. *et al.* Exciton diffusion length in narrow bandgap polymers. *Energy Environ. Sci.* **5,** 6960–6965, doi: 10.1039/c2ee03466b (2012).
19. Zang, H., Ivanov, I. N. & Hu, B. Magnetic studies of photovoltaic processes in organic solar cells. *IEEE* **16,** 1801–1806 (2010).
20. Chen, W., Nikiforov, M. P. & Darling, S. B. Morphology characterization in organic and hybrid solar cells. *Energy Environ. Sci.* **5,** 8045–8074, doi: 10.1039/C2EE22056C (2012).
21. Peet, J. *et al.* Efficiency enhancement in low-bandgap polymer solar cells by processing with alkane dithiols. *Nature Materials* **6,** 497–500, doi: 10.1038/nmat1928 (2007).
22. Price, S. C., Stuart, A. C., Yang, L., Zhou, H. & You, W. Fluorine Substituted Conjugated Polymer of Medium Band Gap Yields 7% Efficiency in Polymer-Fullerene Solar Cells. *J. Am. Chem. Soc.* **133,** 4625–4631, doi: 10.1021/ja1112595 (2011).
23. Walker, B., Kim, C. & Nguyen, T.-Q. Small Molecule Solution-Processed Bulk Heterojunction Solar Cells. *Chem. Mater.* **23,** 470–482, doi: 10.1021/cm102189g (2011).
24. Mishra, A. & Baeuerle, P. Small Molecule Organic Semiconductors on the Move: Promises for Future Solar Energy Technology. *Angew. Chem.-Inter. Edit.* **51,** 2020–2067, doi: 10.1002/anie.201102326 (2012).
25. Sun, Y. *et al.* Solution-processed small-molecule solar cells with 6.7% efficiency. *Nature Mater.* **11,** 44–48, doi: 10.1038/nmat3160 (2012).
26. Zhou, J. *et al.* Small Molecules Based on Benzo 1,2-b:4,5-b' dithiophene Unit for High-Performance Solution-Processed Organic Solar Cells. *J. Am. Chem. Soc.* **134,** 16345–16351, doi: 10.1021/ja306865z (2012).
27. Chi, L.-C. *et al.* Donor-acceptor small molecule with coplanar and rigid pi-bridge for efficient organic solar cells. *Solar Ener. Mater. Solar Cells* **109,** 33–39, doi: 10.1016/j.solmat.2012.10.019 (2013).
28. He, G. *et al.* Efficient small molecule bulk heterojunction solar cells with high fill factors via introduction of pi-stacking moieties as end group. *J. Mater. Chem. A* **1,** 1801–1809, doi: 10.1039/c2ta00496h (2013).
29. Lin, Y. Z., Li, Y. F. & Zhan, X. W. Small molecule semiconductors for high-efficiency organic photovoltaics. *Chem. Soc. Rev.* **41,** 4245–4272, doi: 10.1039/c2cs15313k (2012).
30. Viterisi, A. *et al.* Unambiguous determination of molecular packing in crystalline donor domains of small molecule solution processed solar cell devices using routine X-ray diffraction techniques. *J. Mater. Chem. A* **2,** 3536–3542, doi: 10.1039/c3ta13116e (2014).
31. Kwon, O. K., Park, J.-H., Kim, D. W., Park, S. K. & Park, S. Y. An All-Small-Molecule Organic Solar Cell with High Efficiency Nonfullerene Acceptor. *Adv. Mater.*, n/a-n/a, doi: 10.1002/adma.201405429 (2015).
32. Kyaw, A. K. K. *et al.* Intensity Dependence of Current-Voltage Characteristics and Recombination in High-Efficiency Solution-Processed Small-Molecule Solar Cells. *Acs Nano* **7,** 4569–4577, doi: 10.1021/nn401267s (2013).
33. Zhou, J. Y. *et al.* Solution-Processed and High-Performance Organic Solar Cells Using Small Molecules with a Benzodithiophene Unit. *J. Am. Chem. Soc.* **135,** 8484–8487, doi: 10.1021/ja403318y (2013).
34. Mukherjee, S. *et al.* Importance of Domain Purity and Molecular Packing in Efficient Solution-Processed Small-Molecule Solar Cells. *Adv. Mater.* **27,** 1105–1111, doi: 10.1002/adma.201404388 (2015).
35. Ma, W. *et al.* Quantification of Nano- and Mesoscale Phase Separation and Relation to Donor and Acceptor Quantum Efficiency, Jsc, and FF in Polymer:Fullerene Solar Cells. *Adv. Mater.* **26,** 4234–4241, doi: 10.1002/adma.201400216 (2014).
36. Sweetnam, S. *et al.* Characterization of the Polymer Energy Landscape in Polymer:Fullerene Bulk Heterojunctions with Pure and Mixed Phases. *J Am. Chem. Soc.* **136,** 14078–14088, doi: 10.1021/ja505463r (2014).
37. Wobkenberg, P. H. *et al.* Mesoscale molecular network formation in amorphous organic materials. *Synth. Met.* **158,** 468–472 (2008).
38. Kiel, J. W., Mackay, M. E., Kirby, B. J., Maranville, B. B. & Majkrzak, C. F. Phase-sensitive neutron reflectometry measurements applied in the study of photovoltaic films. *J. Chem. Phys.* **133,** doi: 10.1063/1.3471583 (2010).
39. Staniec, P. A. *et al.* The Nanoscale Morphology of a PCDTBT: PCBM Photovoltaic Blend. *Ad. Ener. Mater.* **1,** 499–504, doi: 10.1002/aenm.201100144 (2011).

40. Sun, Z. Z. *et al.* PS-b-P3HT Copolymers as P3HT/PCBM Interfacial Compatibilizers for High Efficiency Photovoltaics. *Adv. Mater.* **23,** 5529-+, doi: 10.1002/adma.201103361 (2011).
41. Keum, J. K. *et al.* Morphological origin for the stratification of P3HT:PCBM blend film studied by neutron reflectometry. *App. Phys. Lett.* **103,** doi: 10.1063/1.4836035 (2013).
42. Shao, M. *et al.* The isotopic effects of deuteration on optoelectronic properties of conducting polymers. *Nature Comm.* **5,** doi: 10.1038/ncomms4180 (2014).
43. Kiel, J. W., Kirby, B. J., Majkrzak, C. F., Maranvillec, B. B. & Mackay, M. E. Nanoparticle concentration profile in polymer-based solar cells. *Soft Matt.* **6,** 641–646 (2010).
44. Treat, N. D. *et al.* Polymer-fullerene miscibility: a metric for screening new materials for high-performance organic solar cells. *J. Am. Chem. Soc* **134,** 15869–15879 (2012).
45. Shao, M. *et al.* Understanding How Processing Additives Tune the Nanoscale Morphology of High Effi ciency Organic Photovoltaic Blends: From Casting Solution to Spun-Cast Thin Film. *Adv. Ener. Mater.* **24** (42), 6647–6657 (2014).
46. Parratt, L. G. Surface Studies of Solids by Total Reflection of X-Rays. *Phys. Rev.* **95,** 359 (1954).
47. Li, W. *et al.* The Effect of additive on performance and shelf-stability of HSX-1/PCBM photovoltaic devices. *Organ. Elect.* **12,** 1544–1551 (2011).
48. Spano, F. C. The Spectral Signatures of Frenkel Polarons in H- and J-Aggregates. *Acc. Chem. Resea.* **43,** 429–439 (2010).
49. Rau, U. Reciprocity relation between photovoltaic quantum efficiency and electroluminescent emission of solar cells. *Phys. Rev. B* **76,** 085303 (2007).
50. Flory, P. J. *Principles of Polymer Chemistry*. (Cornell University Press, 1953).
51. Carrillo, J. M. Y., Kumar, R., Goswami, M., Sumpter, B. G. & Brown, W. M. New Insights into Dynamics and Morphology of P3HT:PCBM Active Layers in Bulk Heterojunctions. *Phys. Chem. Chem. Phys.* **15,** 17873 (2013).

Acknowledgements

N.H., J.Z. P.J. acknowledge support of ORNL Laboratory Research and Development Program (LDRD) project. This research was conducted at the Center for Nanophase Materials Sciences and the Spallation Neutron Source, which are sponsored by the Scientific User Facilities Division, Office of Basic Energy Sciences, U.S. Department of Energy. N.H. thanks Artur Glavic, Haile Ambaye and Richard Goyette for a partial assistance during the NR measurements. This manuscript has been authored by UT-Battelle, LLC under Contract No. DE-AC05-00OR22725 with the U.S. Department of Energy. The Department of Energy will provide public access to these results of federally sponsored research in accordance with the DOE Public Access Plan (http://energy.gov/downloads/doe-public-access-plan).

Author Contributions

N.H. designed the experiment, prepared the samples, performed NR, XRD, XR, AFM experiments, analyzed the data and wrote portions of the paper. V.L. designed the study, performed NR experiments, and the data analysis and supervised the research. J.F.B. performed NR experiments. S.D. and K.X. prepared solar cells and characterized solar cells. J.K.K. assisted in measuring XRD and XRR experiments. J.Z. and I.N.I. obtained and analyzed optical properties of solutions and films. R.K. and B.G.S. carried out theoretical calculations. J.K.K., J.Z., I.N.I. and R.K. contributed to writing sections of the paper. All authors contributed with discussion, feedback and comments on the manuscript.

Additional Information

Supplementary information accompanies this paper at http://www.nature.com/srep

Competing financial interests: The authors declare no competing financial interests.

How to cite this article: Herath, N. *et al.* Peculiarity of Two Thermodynamically-Stable Morphologies and Their Impact on the Efficiency of Small Molecule Bulk Heterojunction Solar Cells. *Sci. Rep.* **5**, 13407; doi: 10.1038/srep13407 (2015).